

Efficiency study of PbTe/CdTe Core/Shell quantum dots solar cells

Estudo da eficiência em células solares de pontos quânticos do tipo Core/Shell de PbTe/CdTe

Silvio José Prado¹

Abstract

In this work we theoretically study how to optimize the efficiency of an intermediate band solar cell based on IV-VI PbTe/CdTe semiconductor materials. We focus our attention on how control structural parameters, such as the height and radius in cylindrical quantum dots and the radius in spherical quantum dots to obtain the inter and intraband transition energies that provide the highest efficiency values of the solar cell. The calculation of the energy levels, the selection rules for transitions energies were performed using the 4×4 $\mathbf{k.p}$ Kane-Dimmok Hamiltonian.

Keywords: Quantum dots. Solar cell. Efficiency. Geometry. Kane-Dimmok Hamiltonian.

Resumo

Neste trabalho estudamos teoricamente como otimizar a eficiência de uma célula solar de banda intermediária baseada em pontos quânticos de materiais semicondutores IV-VI de PbTe/CdTe. Focamos nossa atenção em como controlar os parâmetros estruturais, como a altura e o raio no ponto quântico cilíndrico e o raio no ponto quântico esférico para obter as energias de transição inter e intrabanda que forneçam os maiores valores de eficiência da célula solar. O cálculo dos níveis de energia e das regras de seleção das energias de transições foi realizado usando o Hamiltoniano $\mathbf{k.p}$ 4×4 de Kane-Dimmok.

Palavras-chave: Pontos quânticos. Células solares. Eficiência. Geometria. Hamiltoniano Kane-Dimmok.

¹Prof. Dr. in Physics, Pontal Institute of Exact and Natural Sciences–ICENP–UFU, Minas Gerais, Brazil; E-mail: sprado@ufu.br

Introduction

Intermediate band solar cells (IBSCs) are high efficiency solar cells based on the introduction of an intermediate band (IB) between the valence band (VB) and the conduction band (CB) of a semiconductor material. In this configuration, IB produces an increase in photocurrent through the absorption of photons by the two subbands, in which a single photon promotes an electron from VB to IB and a second photon promotes an electron from IB to CB, thus creating a single electron-hole pair (MELLOR *et al.*, 2013). In this type of nanostructured system, it is possible to control the electronic structure through structural parameters such as size or tension, the geometric shape of the quantum dots (QDs) which modifies the symmetry of quantum states, with the action of external fields, and the appropriate choice of materials that form the nanostructure.

In the context of IBSCs, quantum dots based on type III-V semiconductor materials such as InGaAs/AlGaAs have been extensively studied. In more recent years the focus of research has been on the use of materials such as InPsb/AlAsSb, GaAsSb/AlAsSb, QDs of lead salts, IV-VI, such as PbTe, PbSe and PbS (ANTOLÍN; MARTÍ; LUQUE, 2011; GOODWIN *et al.*, 2018; ZIHAN *et al.*, 2018), as well as the search for new materials that allow a great efficiency in photovoltaic conversion (KABALAN; SINGH, 2017; JEEVANANDAM *et al.*, 2020).

An important factor in the physics of quantum dot IBSCs is a clear understanding of the intra-band optical transitions in these systems. In the case of transitions between the bounded states (BS) associated with the presence of the QD and the extended states (EE) in the CB, a good approximation can be obtained using the multiband $\mathbf{k}\cdot\mathbf{p}$ method. Approximations using a single band do not include important effects such as the mixing of holes, the coupling between holes and electrons and an appropriate discussion of states of symmetry and their impact on optical transitions (PRADO *et al.*, 2012; PRADO; MARQUES; ALCALDE, 2017).

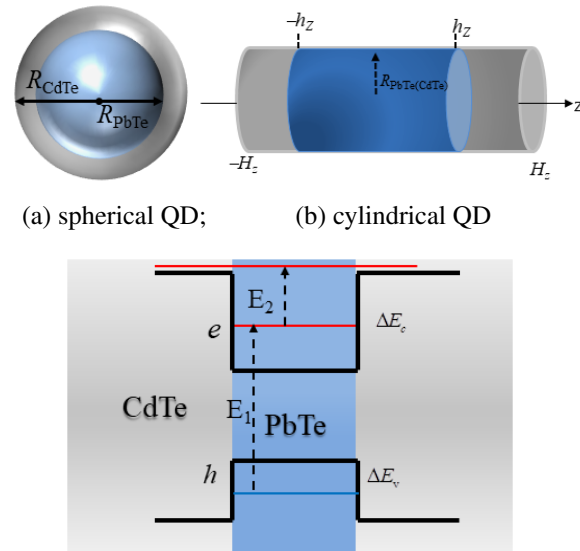
This paper is dedicated to studying the relevant parameters in the QD-IBSCs such as photocurrent and photovoltaic efficiency. The discussion is based on the $\mathbf{k}\cdot\mathbf{p}$ Kane-Dimmock Hamiltonian (KANG; WISE, 1997) applied to PbTe/CdTe core/shell QDs, of different sizes and geometries.

Material and methods

Theory

Figure 1 shows a schematic representation of the QDs, where in letter Figure 1(a) we have spherical QD, showing PbTe core and CdTe shell. The difference between R_{CdTe} and R_{PbTe} is the thickness of the shell of the CdTe. Figure 1(b) is for a cylindrical QD, where H_z is the half-height of the largest cylinder (shell) and h_z is the half-height of the QD (core) and R is the radius of the core and shell. Finally, Figure 1(c) shows a scheme of the energy levels of the valence band, the intermediate band, conduction band and the interband transition energy E_1 and intraband transition energy E_2 .

Figure 1 – Schematic representation of the QD systems shows



(a) spherical QD; (b) cylindrical QD

(c) representation of the energy bands for two geometries, which the offsets of the conduction (ΔE_c) and valence (ΔE_v) bands and the transitions between VB to IB and from this to BC.

Source: The author.

To describe a carrier in the presence of a V confinement potential, we use the 4×4 $\mathbf{k}\cdot\mathbf{p}$ Kane-Dimmock model, which takes exactly into account the interactions between the L_6^- and L_6^+ bands, moreover the diagonal solutions of this Hamiltonian were used to describe the four-component spinor ψ (TUDURY *et al.*, 2020),

$$H_{k,p} = \begin{bmatrix} E_g - D_1^- & \frac{\hbar P_1}{m_0} P_z & 0 & \frac{\hbar P_1}{m_0} P_- \\ \frac{\hbar P_1}{m_0} P_z & D_2^+ & \frac{\hbar P_1}{m_0} P_- & 0 \\ 0 & \frac{\hbar P_1}{m_0} P_+ & E_g - D_1^- & \frac{\hbar P_1}{m_0} P_z \\ \frac{\hbar P_1}{m_0} P_+ & 0 & \frac{\hbar P_1}{m_0} P_z & D_2^+ \end{bmatrix} \quad (1)$$

where, for $i = 1, 2$

$$D_i^\pm = -\hbar^2 \nabla^2 / 2m_i^\pm + C_i P_z^2,$$

and

$$C_1 = \hbar^2 / 2 (1/m_i^- - 1/m_i^+),$$

$$C_2 = \hbar^2 / 2 (1/m_i^+ - 1/m_i^-),$$

are the effective mass of electrons and holes, while P_l e P_l are the anisotropic conduction-valence coupling parameters Kane-Dimmock for the longitudinal and transverse directions. The operators P_z and $P_\pm = P_x \pm iP_y$ are defined as $\partial/\partial z$ and $\partial/\partial x \pm i\partial/\partial y$ and m_0 is the mass of free electron.

In general, each component of the spinor in spherical coordinates has the form $f_n^L(r, \Omega) = A_{n,L} j_L(k_n^L r) Y_L^M(\Omega)$ where $A_{n,L}$ is a normalization constant, $j_L(x)$ is the spherical Bessel function, and $Y_L^M(\Omega)$ the spherical harmonics. The wave functions $\psi_{I(II)}$ for subspaces I and II of different parities can be written as a linear combination of the envelope functions $f_n^L(r, \Omega)$ and the four Bloch functions at the L -point (PRADO *et al.*, 2012), as

$$|\psi_{I(II)}^M\rangle = \sum_n \sum_{L \geq |M|}^\infty \begin{pmatrix} C_{n,2L(2L+1)}^M f_{n,2L(2L+1)}^M | L_6^- \uparrow \rangle \\ C_{n,2L+1(2L)}^M f_{n,2L+1(2L)}^M | L_6^+ \uparrow \rangle \\ C_{n,2L(2L+1)}^{M+1} f_{n,2L(2L+1)}^{M+1} | L_6^- \downarrow \rangle \\ C_{n,2L+1(2L)}^{M+1} f_{n,2L+1(2L)}^{M+1} | L_6^+ \downarrow \rangle \end{pmatrix} \quad (2)$$

For cylindrical geometry, the spinor has the following form

$$F_{n,L,m}^\pm(\rho, \phi, z) = B_{n,L} J_L(k_n^L \rho) \left(\frac{e^{iL\phi}}{\sqrt{2\pi}} \right) f^\pm(m, z),$$

where $B_{n,L}$ is a normalization constant and J_L is the Bessel function. The dependent term in z is given by,

$$f^\pm(m, z) = \left(1/\sqrt{H_z} \right) \text{sen}[m\pi(1/2 - z/H_z)],$$

with H_z being half-height of the large cylinder, as shown in Figure 1(b). The signs in the expression for $f^\pm(m, z)$ correspond to symmetry with m even, plus signal and odd, minus signal. The wave functions in this case are divided into four subspaces $\psi_{I(II)}$ and $\psi_{III(IV)}$, of different parities, given by,

$$|\psi_{I(II)}^m\rangle = \sum_{n,L,M} \begin{pmatrix} C_{n,2L(2L+1)}^- f_{n,2L(2L+1)}^- | L_6^- \uparrow \rangle \\ C_{n,2L(2L+1)}^+ f_{n,2L(2L+1)}^+ | L_6^+ \uparrow \rangle \\ C_{n,2L+1(2L)}^+ f_{n,2L+1(2L)}^+ | L_6^- \downarrow \rangle \\ C_{n,2L+1(2L)}^- f_{n,2L+1(2L)}^- | L_6^+ \downarrow \rangle \end{pmatrix} \quad (3)$$

$$|\psi_{III(IV)}^m\rangle = \sum_{n,L,M} \begin{pmatrix} C_{n,2L+1(2L)}^+ f_{n,2L+1(2L)}^+ | L_6^- \uparrow \rangle \\ C_{n,2L+1(2L)}^- f_{n,2L+1(2L)}^- | L_6^+ \uparrow \rangle \\ C_{n,2L(2L+1)}^- f_{n,2L(2L+1)}^- | L_6^- \downarrow \rangle \\ C_{n,2L(2L+1)}^+ f_{n,2L(2L+1)}^+ | L_6^+ \downarrow \rangle \end{pmatrix} \quad (4)$$

where the coefficients $C_{n,L}^{M(\pm)}$, in equations (1) and (2), are constants to be determined.

The wave functions of electrons and holes must satisfy the following boundary conditions;

- (i) in the spherical QD, in the PbTe/CdTe interface, that is, in R_{PbTe} the potential is finite, and the values are given by the offsets of the conduction and valence bands, and in the radius of the CdTe, R_{CdTe} , the potential is infinite and the wave function must be canceled,
- (ii) for the cylindrical QD the potential discontinuity occurs in $\pm h_z$ and the wave function is canceled in R and in $\pm H_z$.

The probability of optical transition is proportional to the matrix element of the crystal-radiation interaction,

$$\langle \psi_{e,j} | \hat{\mathbf{e}} \cdot \hat{\mathbf{P}} | \psi_{h,j'} \rangle = j, j' = I, II$$

for the spherical QD and $j, j' = I(II), III(IV)$, for the cylindrical QD. Here, $\hat{\mathbf{e}}$ is the polarization vector of light and $\hat{\mathbf{P}}$ is the momentum operator.

Using equations (1) and (2), the matrix elements above can be written as,

$$\begin{aligned} \langle \psi_{e,j}^{M_e(m_e)} | \hat{\mathbf{e}} \cdot \hat{\mathbf{P}} | \psi_{h,j}^{M_h(m_h)} \rangle &= \\ &= \sum_{\alpha, \alpha'} \langle f_{e,\alpha}^{M_e(m_e)} | f_{e,\alpha'}^{M_h(m_h)} \rangle \langle \mu_\alpha | \hat{\mathbf{e}} \cdot \hat{\mathbf{P}} | \mu_{\alpha'} \rangle \\ &+ \langle \mu_\alpha | \mu_{\alpha'} \rangle \langle f_{e,\alpha}^{M_e(m_e)} | \hat{\mathbf{e}} \cdot \hat{\mathbf{P}} | f_{e,\alpha'}^{M_h(m_h)} \rangle. \end{aligned} \quad (5)$$

The conduction band states (valence) are written as,

$$f_{e,\alpha}^{M_e(m_e)} \left(f_{h,\alpha}^{M_h(m_h)} \right)$$

with α representing the quantum numbers n, L and μ_α is the periodic Bloch functions at point L for each carrier and for each QD geometry. The first term of equation (3) and of the equation (4) is responsible for interband transitions. In our case the complete set of selection rules are obtained from the non-null terms of the products of the matrix elements

$$I_{e,h} \delta_{L_e, L_h} \Pi_{\alpha, \alpha'},$$

where $\Pi_{\alpha,\alpha'}$ is the matrix parity operator, and

$$I_{e,h} = \left\langle f_{e,\alpha}^{M_e(m_e)} \left| f_{h,\alpha'}^{M_e(m_e)} \right. \right\rangle$$

is the overlap integral of the electron-hole envelope functions allowed transitions. The second term on the equation (5) describe the intraband transitions, since

$$\langle \mu_\alpha | \mu_{\alpha'} \rangle = \delta_{jj'},$$

and the incident light couples, in the same band, state with different symmetries since the term

$$\langle f_j | \hat{\mathbf{e}} \cdot \hat{\mathbf{p}} | f_{j'} \rangle$$

be non-null for a given polarization. These selection rules allow for transitions between states of different parities, or equivalently, when the initial and final states belong to different Hilbert subspaces, equations (2)-(4), and apply to both geometries of QDs.

The next step is to calculate the optical absorption coefficient for non-polarized incident light, which can be written as,

$$\begin{aligned} \alpha(\hat{\mathbf{e}}, \omega) = & \frac{\alpha_0 \Gamma}{\pi} \sum_{N_{h(e)}, N_e, M} \{I \leftrightarrow II\} + \\ & + \frac{\alpha_0 \Gamma}{\pi} \sum_{N_{h(e)}, N_e, M} \frac{\left| F_{N_e, M}^{N_h, M'}(I, II) \right|^2 \left(\left| G_{N_e, M(m)}^{N_e, M'(m')} (I, II) \right|^2 \right)}{\left[(E_{N_e, M}(I) - E_{N_{h(e)}, M}(II) - \hbar\omega)^2 + \Gamma^2 \right]} \end{aligned} \quad (6)$$

where α_0 is the normalization constant, ω is the frequency of the incident light and Γ is the scattering constant. The terms,

$$F_{N_e, M(m)}^{N_h, M'}$$

and

$$G_{N_e, M(m)}^{N_e, M'(m')}$$

represent the inter and intraband oscillator strength, respectively (PRADO *et al.*, 2012; PRADO, 2020). It should note that in equation (5), appear subspaces I and II , however for cylindrical geometry transitions can occur between $I(II)$ to $III(IV)$ subspaces.

The photocurrent density was calculated using the following expression

$$J_{BV \rightarrow BI \rightarrow BC}^{max} = \int_{E < E_C} q \Phi_{T_s} \left(1 - e^{-\alpha_{BV \rightarrow BI \rightarrow BC}^{max} L} \right) dE, \quad (7)$$

where $L = R_{PbTe} + R_{CdTe}$, for the spherical QD and $L = 2H_z$ for the cylindrical QD, α is the total absorption coefficient given by equation (6). Φ_{T_s} is the solar flux modeled as blackbody radiation with the sun at a temperature T_s . The efficiency of the solar cell (η), in turn, is the

ratio of the output power delivered by the cell (P) divided by the power produced by the sun incident on the solar cell (P_s), that is, $\eta = P/P_s$. The power of the sun, P_s is constant and is related to the temperature of the sun, T_s , and F is the geometric factor, which considers the angular dependence on radiation. A circuit delivers a power density that is given by $P = JV$, where J is the current density at some voltage V . Thus, the determination of $\eta = JV/P_s$ is reduced to the calculation of the current density J .

Some assumptions must be done to calculate the current density:

- (i) the sun and solar cell behave like black bodies at different temperatures;
- (ii) direct radioactive transitions are dominant, non-radioactive transitions are ignored;
- (iii) all photons with energy above the gap are absorbed;
- (iv) the quasi-Fermi levels are constant;
- (v) a single electron-hole pair is created per photon. Following the above considerations, the absorption of energy from the sun by the photocell must be equal to the energy irradiated by the cell to the sun (PRADO; MARQUES; ALCALDE, 2017).

Results

The parameters used in the \mathbf{k}, \mathbf{p} model to calculate the electronic structure can be found in Tudury (2000). The energy gap for P_{bTe} is 320meV and for C_{dTe} is 1510meV, both at temperature of 300K. The effective transverse and longitudinal masses of electrons (holes) for P_{bTe} ; $m_t = 10.73m_0$ ($= 0.41m_0$) and $m_l = 1.2m_0$ ($= 0.7m_0$), and finally the transversal and longitudinal coupling parameters between the conduction and valence bands, $P_t = 46.0$ meV and $P_L = 14.0$ meV, respectively.

The conduction and valence band-offsets are given by:

$$\Delta E_C = 90\% (E_{G, CdTe} - E_{G, PbTe})$$

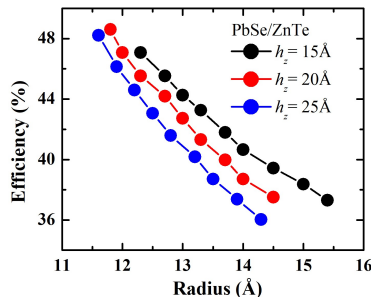
and

$$\Delta E_V = 10\% (E_{G, CdTe} - E_{G, PbTe}),$$

respectively.

Figure 2 shows the results of the efficiency for a cylindrical QD, as a function of the radius (R) and for three values of the half-height (h_z) of the PbTe. These results were obtained, fixing h_z in 200Å and varying both R and h_z , with the objective of obtaining a single energy level in IB, because a dense spectrum of energy levels, can eventually degrade the optical absorption of the system directly affecting efficiency.

Figure 2 – Efficiency for the PbTe/CdTe cylindrical QD as a function of radius, for three different h_z values. The lines are guides for the eyes.



Source: The author.

We observed in these results that the efficiency increases with the reduction of the radius in all the values of h_z , in addition it presents an almost linear dependence with the radius. The maximum value for $\eta = 45.0\%$ in $h_z = 20\text{Å}$ and $R = 13.3\text{Å}$.

This behavior can be understood by observing that in equation (7), used to calculate the current density, the exponential is related to the absorption coefficient, which in turn has a dependence on the inverse of the transition energies, equation (6). So as expected, increasing the spatial confinement, increasing the separation between the energy levels of the carriers, which directly influences the current density and, consequently, the efficiency. The same behavior can be seen by setting R value and following h_z , when it decreases the efficiency increases.

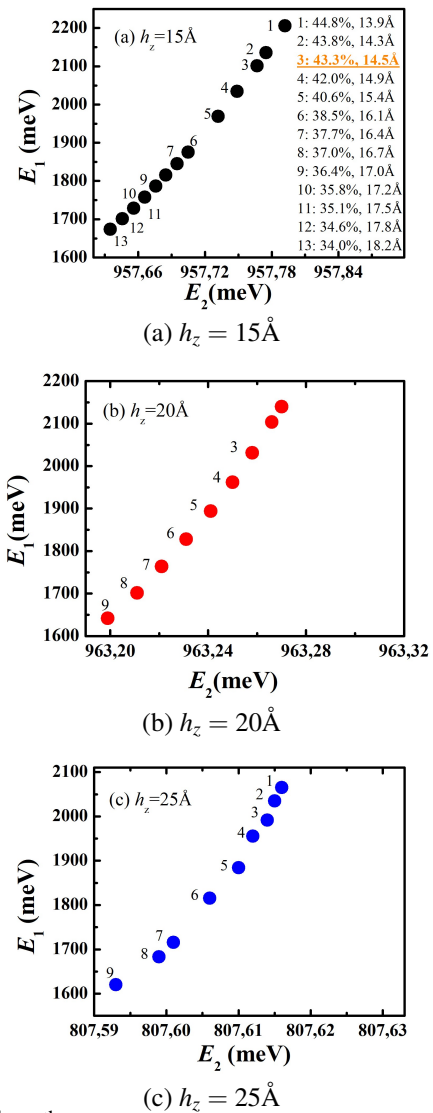
The results in Figure 3(a)-(c), show the same efficiency values of the Figure 2, for a cylindrical QD, now as a function of the transition energies, E_1 , from the VB to IB and E_2 , from IB to CB. As discussed in the results of Figure 2, the energies E_1 and E_2 increase in values when the confinement of the carriers increases and the efficiency reaches maximum values in the lowest R for each h_z values, 15Å , 20Å and 25Å .

The highlighted values in orange in Figures 3(a)-(c), are for cylindrical QDs with the same values of radius, $R = 14.5\text{Å}$, and allow us to see that the efficiency is greater in Figure 3(a) where the energies E_1 and E_2 are higher because $h_z = 15\text{Å}$, showing again the confinement effect, in this case in z -direction.

The results for the spherical geometry, as a function of the radius and as a function of the transition energies E_1 and E_2 , are shown in Figures 4 and 5, respectively.

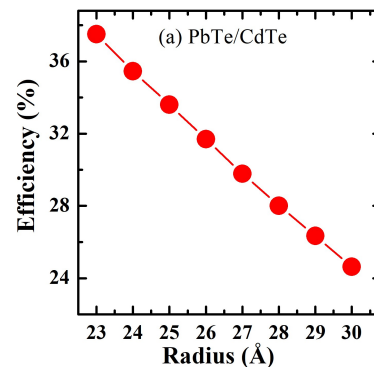
These results show the same type of efficiency behavior as the case of the cylindrical QD, both as a function of the radius and as a function of the transition energies. However, the maximum efficiency is 35.0% at $R = 23\text{Å}$, that is, less than in the cylindrical QD.

Figure 3 – Efficiencies as a function of the transition energies from the valence band to the intermediate band (E_2) and from the intermediate band to the conduction band (E_1), for the PbTe/CdTe cylindrical QDs. On the right are the efficiency and radius values.



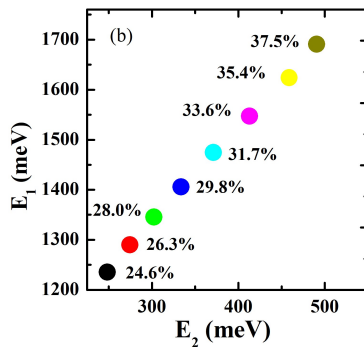
Source: The author.

Figure 4 – Efficiencies for the PbTe/CdTe QDs, as a function of the radius.



Source: The author.

Figure 5 – Efficiencies for the PbTe/CdTe QDs, as a function of the transition energies E_1 and E_2



Source: The author.

The change in the geometry of the quantum dots from cylindrical to spherical, affects differently the spatial confinement of the carriers, whereas in the first geometry we have two parameters that can be controlled, h_z and R , allowing a fine adjustment of the transition energy in order to maximize the efficiency, in spherical geometry we have only parameter to control the confinement, which is the radius of the QD.

Conclusion

In conclusion, we theoretically study the potential application of different geometry of QDs in PbTe/CdTe intermediate band solar cells.

Using the $\mathbf{k}\cdot\mathbf{p}$ method we carry out a systematic study exploring the structural parameters such as, height and radius in cylindrical QDs, and radius in spherical QDs, to obtain maximum efficiency in this type of solar cells with one intermediate band produced by QDs. The numerical results show that is possible to achieve great efficiencies in a restricted set of parameters values, R and h_z , whose correct determination can allow the implementation of this type of semiconductors QDs solar cells.

Acknowledgments

The author would like to thank ICENP, Instituto de Ciências Exatas e Naturais do Pontal, UFU, for support.

References

- ANTOLÍN, E.; MARTÍ, A.; LUQUE, A.; The lead salt quantum dot intermediate band solar cell, *IEE*, v. 978, p. 001907, 2011.
- GOODWIN, H.; JELICOE, T. C.; DAVIS, N. J. L. K.; BÖHM, M. L. Multiple exciton generation in quantum dot-based solar cells, *Nanophotonics*, Berlin, v. 7, n. 1, p. 111–126, 2018.
- JEEVANANDAM, J.; BALU, S. K.; ANDRA, S.; DANQUAH, M. K.; VIDYAVATHI, M.; MUTLALAGU, M.; Quantum dots synthesis and application, *In*: MUBARAK, N. M.; KALID M., WALVEKAR, R.; NUMAN, A. (eds), Contemporary nanomaterials in material Engineering applications, *Engineering materials*. Springer, 2020.
- KABALAN, A. A.; SINGH., P.; CdTe/PbTe superlattice modeling and fabrication for solar cells applications, *Journal of Nano Research*, v. 48, p. 125-137, 2017.
- KANG, I.; WISE, F. W.; Electronic structure and optical properties of PbS and PbSe quantum dots, *J. Opt. Soc. Am. B*, v. 14, n. 7, 1997.
- MELLOR, A.; LUQUE, A.; TOBÍAS, I.; MARTÍ, A.; A numerical study into the influence of quantum dot size on the sub-bandgap interband photocurrent in intermediate band solar cells, *AIP Advances*, v. 3, p. 022116, 2013.
- PRADO, S. J. VILLEGAS-LELOVSKY, L., ALCALDE, A. M., LOPEZ-RICHARD, V., MARQUES, G. E. Magneto-optical properties in IV-VI lead-salt semimagnetic nanocrystals. *Nanoscale Research Letters*, v. 7, p. 374, 2012.
- PRADO, S. J.; MARQUES, G. E.; ALCALDE, A. M.; Photovoltaic efficiency of intermediate band solar cells based on CdTe/CdMnTe coupled quantum dots. *J. Phys.: Condens. Matter*, [S. l.], v. 29, p. 445301, 2017. DOI: <https://doi.org/10.1088/1361-648X/aa85c7>.
- PRADO, S. J. Study of the optical properties in charged CdTe quantum dots. *Semina: Exact and Technological Sciences*, v. 41, n. 1, p. 205-2010, 2020. DOI: <https://doi.org/10.5433/1679-0375.2020v41n2p205>.
- TUDURY, G. E.; MARQUEZINI, M. V.; FERREIRA, L. G.; BARBOSA, L. C.; CESAR, C. L.; Effect of band anisotropy on electronic structure of PbS, PbSe, and PbTe quantum dots, *Physical Review B*, v. 62, p. 7357, 2000.
- ZIHAN, C.; ZHILONG, Z.; JIANFENG, Y.; WEIJAN, C.; ZHI, L. T.; DIAN, W.; LIN, Y.; JIANBING, Z.; JOHN, S.; GAVIN, J. C.; ROBERT, J.; PATTERSON, S. Improving carrier extraction in a PbSe quantum dot solar cell by introducing a solution-processed antimony-doped SnO₂ buffer layer. *Journal of Materials Chemistry C*, Cambridge, v. 37, p. 9861-9866, 2018.

Received: May 2, 2021
Accepted: June 28, 2021
Published: June 30, 2021